Maximum Power per Ampere Modulation for Cascaded H-Bridge Converters

Ivan Spina, Daniel J. Rogers, *Senior Member, IEEE*, Gianluca Brando, Efstratios Chatzinikolaou, and Yam P. Siwakoti, *Senior Member, IEEE*

***Abstract*— This article shows how to exploit the degree of freedom represented by the common-mode voltage, which is inherent in three-phase Cascaded H-bridge (CHB) converters, to minimize the total rms current value of the distributed dc sources. An optimal common-mode voltage injection law is derived, constituting a maximum power per ampere (MPPA) modulation strategy with respect to the currents of the dc sources. The potential benefits introduced by the proposed algorithm are analyzed in the context of battery-fed CHB converters and validated experimentally with a three-time-constant Randles model of a battery cell. The MPPA strategy is compared with traditional common-mode voltage injection methods, and battery loss reduction is demonstrated. The obtained ES is dependent on the converter *m* and power factor. Experimental tests on a 36-cell full-bridge CHB converter validate the simulation and numerical derivation. To demonstrate the efficacy of the proposed method in practical applications, a 3 MW energy storage system (ESS) and a 110 kW battery electric vehicle (BEV) undergoing standard drive cycles are presented as case studies. Compared to traditional modulation strategies, the MPPA strategy reduces the battery losses by up to 10.9% in the ESS and 27.5% in the BEV application.**

***Index Terms*— Battery energy storage, cascaded H-bridge (CHB), maximum power per ampere (MPPA).**

Nomenclature

E_{bl} :	Total battery energy loss.
ES :	Battery energy saving.
f :	Objective function.
I :	Peak ac current amplitude.
I_b :	Total root mean square (rms) battery current.
$I_{b,\text{dc}}$:	Total dc component battery current.
$I_{b,\text{dc},k,n}$:	DC component current value of the nth battery in the kth phase.
$i_{b,k,n}$:	Current of the nth battery in the kth phase.
$I_{b,k,n}$:	rms current value of the nth battery in the kth phase.
i_k:	kth phase current.
m :	Modulation index.
$M_{k,n}$:	nth module of the kth phase.
N :	Number of modules per arm.
$N_{k,\text{IN}}$:	Number of inserted batteries within the generic arm k.
P_{bl} :	Total battery power loss.
$P_{\text{bl},k,n}$:	Battery power loss of the nth battery in the kth phase.
ρ :	Derivative of f with respect to v_o^*.
φ :	Current angle delay.
ω :	Fundamental output angular frequency.
V_b :	Battery voltage.
v_{dk} :	Differential-mode voltage component.
v_k :	Voltage of the kth phase.
v_o :	Common-mode voltage component.
$v_{o,\text{bal}}$:	Common-mode voltage component at the fundamental frequency for inter-arm balancing action.
$v_{\text{omin}}, v_{\text{omax}}$:	Minimum and maximum limits for the common-mode voltage component.
$*$:	Superscript for reference quantities.
k :	Subscript referring to the converter phase ($k = 1, 2, 3$).
n :	Subscript referring to the converter module ($n = 1, \ldots, N$).

Manuscript received 7 April 2021; revised 16 August 2021; accepted 9 September 2021. Date of publication 20 September 2021; date of current version 3 February 2023. This work was supported in part by U.S. Department of Commerce under Grant BS123456. Recommended for publication by Associate Editor Zhongbao Wei. *(Corresponding author: Yam P. Siwakoti.)*

Ivan Spina and Gianluca Brando are with the Department of Electrical Engineering and Information Technology, University of Naples Federico II, 80125 Naples, Italy (e-mail: ivan.spina@unina.it; gianluca.brando@unina.it).

Daniel J. Rogers and Efstratios Chatzinikolaou are with the Power Electronics Group, Department of Engineering Science, University of Oxford, Oxford OX1 3PJ, U.K. (e-mail: dan.rogers@eng.ox.ac.uk; stratos_hatz@hotmail.com).

Yam P. Siwakoti is with the Faculty of Engineering and Information Technology, University of Technology Sydney, Sydney, NSW 2007, Australia (e-mail: yam.siwakoti@uts.edu.au).

Color versions of one or more figures in this article are available at https://doi.org/10.1109/JESTPE.2021.3114005.

Digital Object Identifier 10.1109/JESTPE.2021.3114005

I. Introduction

MODULAR converters offer distinct advantages over conventional voltage source inverters (VSIs) and, indeed, numerous authors have proposed this solution for various applications, including variable-speed drives [1], [2], energy storage systems (ESSs) [3], [4], and wind turbines [5], [6]. The high-quality output waveform produces low electromagnetic interference (EMI), and switching losses are low, especially when the nearest level control (NLC) modulation technique is used [7]. It has been shown that battery-fed solutions can be used to achieve accurate state of charge (SoC) balancing even between severely mismatched batteries [8], [9]. Modular converters also offer inherent scalability to higher voltages because of their redundancy and ability to dynamically isolate failed modules from a larger series string [10], [11].

2168-6777 © 2021 IEEE. Personal use is permitted, but republication/redistribution requires IEEE permission.
See https://www.ieee.org/publications/rights/index.html for more information.

Authorized licensed use limited to: Universita degli Studi di Napoli Federico II. Downloaded on August 12,2026 at 12:04:15 UTC from IEEE Xplore. Restrictions apply.

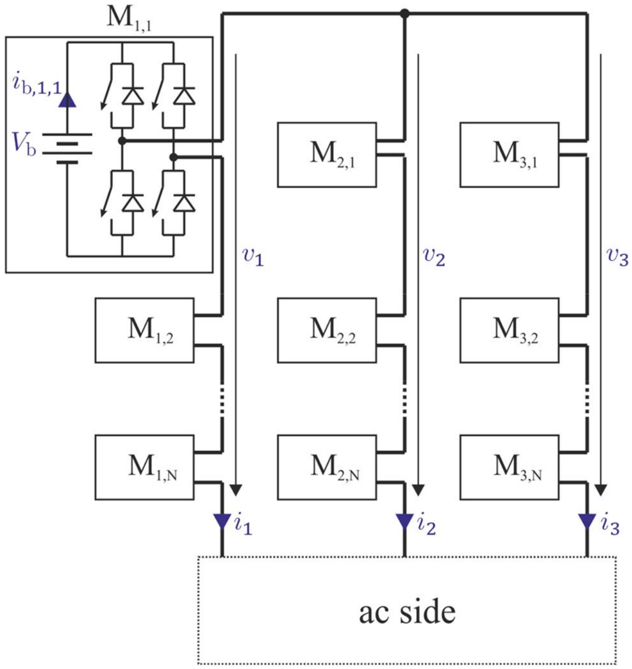

Fig. 1. Three-phase battery-fed CHB converter.

Cascaded H-bridge (CHB) converters [12] are based on the cascaded connection of full-bridge choppers, each unit embedding a dc source. The dc source can be of various types including capacitor, supercapacitor, battery, and fuel cell. The chopper and its dc source constitute one module, and the series connection of modules constitutes one arm. In this work, we use the term CHB to represent the three-phase converter obtained by the single-star connection of three arms,[1] each arm is realized by the series connection of full-bridge choppers embedding a dc source, as shown in Fig. 1.

In a cascaded converter, each dc source is switched in and out of the conduction path depending on the instantaneous arm voltage required. This naturally leads to a pulsed current flowing in the dc sources of each module [14]. As a result, the dc sources are subjected to a low-frequency (LF) current ripple. Considering that any real dc source (e.g., battery) is characterized by resistive internal parameters, this will lead to power loss [15]. This relative increase of rms current value for a given average power transfer cannot be eliminated entirely without introducing an additional energy buffer between the dc sources and the choppers to filter the pulsating power, which would entail additional cost and complexity in the circuit.

Although the literature recognizes the common-mode voltage shared by all phases as a degree of freedom for modular multilevel converters (MMCs) [16], there has been no analysis of its effect on the current experienced by the dc sources. To-date, the injection of the common-mode voltage has been exploited only for converters equipped with capacitors [17]–[19] in order to influence capacitor voltage ripple, or for the inter-arm balancing of battery-fed systems [20], and maximizing the linear modulation region [21]. As battery-fed modular converters are being proposed for both ESSs [3], [4] and battery electric vehicles (BEVs) [22], [23], a method to reduce battery losses would improve the efficiency and lifetime performance of these systems.

This article explores the influence of the common-mode reference voltage in rms current value experienced by the dc sources of a CHB converter. An optimized common-mode voltage injection law is derived to minimize the dc sources rms current value. The proposed technique constitutes a discontinuous modulation strategy that realizes a maximum power per ampere (MPPA) control of the converter with respect to the currents of its distributed dc sources.

For battery-fed CHB converters, this work evaluates the potential ES introduced by the proposed method by means of an experimentally validated Randles dynamic $3p3z$ battery cell model [23]. Experiments on a three-phase 36 cell CHB converter laboratory prototype validate the mathematical derivation, demonstrating a substantial reduction of rms battery current. Two case studies, a 3 MW ESS and a 110 kW BEV, are used to evaluate the benefits introduced by the proposed algorithm in real-world applications. In both cases, significant battery loss reductions are observed.

This article is organized as follows. Section II presents the description of the overall system, followed by a detailed explanation of the proposed MPPA strategy in Section III. Sections IV and V discuss and compare the proposed method with the traditional method. Simulations and experimental results are presented in Section VI for verification and finally concluded in Section VII.

II. Description of the System

Fig. 1 shows the three-phase CHB converter, consisting of three arms and interfaced with the ac side, which can either be a three-phase passive load or the ac grid. Each arm is realized by N series connected H-bridge modules embedding a battery of voltage V_b. The modules have been enumerated as $M_{k,n}$ where the subscript k represents the converter phase ($k = 1, 2, 3$) and $n = 1, \ldots, N$. The total arm voltages and currents are denoted respectively with v_1, v_2, v_3 and i_1, i_2, i_3, while $i_{b,k,n}$ represents the current of nth battery in the kth phase.

According to the status of the switches in the module, the output voltage of the module can be V_b, 0 or $-V_b$, and by suitable control of the switches in all modules, a quantized voltage in the range $\pm N V_b$ can be generated in each phase. The generic arm voltage reference can be modulated by means of either pulse width modulation (PWM) or NLC techniques [22].

The common-mode reference voltage is defined as the instantaneous average of the arm voltages

$$v_o^* = \left(v_1^* + v_2^* + v_3^*\right)/3 \tag{1}$$

where v_1^*, v_2^*, v_3^* are the reference voltages of the three arms.

[1]For brevity, in this work the term CHB is used to describe the specific three-phase single-star arrangement. However, in other contexts, CHB is a broad term that can also refer to other arrangements of arms that contain full-bridge modules. For example, [13] classifies several circuits that are all referred to as CHB converters.

Authorized licensed use limited to: Universita degli Studi di Napoli Federico II. Downloaded on August 12,2026 at 12:04:15 UTC from IEEE Xplore. Restrictions apply.

Thus, the generic arm voltage reference v_k^* can be decomposed in its differential and common-mode components

$$\begin{cases} v_1^* = v_{d1}^* + v_o^* \\ v_2^* = v_{d2}^* + v_o^* \\ v_3^* = v_{d3}^* + v_o^* \end{cases} \tag{2}$$

where v_{dk}^* is the differential component of v_k^*.

Naturally, the common-mode voltage does not modify the line-to-line voltages. In three-phase three-wire systems the ac currents only depend the line-to-line voltages. Therefore, v_o^* represents a degree of freedom of the modulation process.

Considering that $v_k^* \in [-NV_b, NV_b]$, the voltage v_o^* has to be kept in the range $\left(v_{\text{omin}}^*, v_{\text{omax}}^*\right)$, with

$$\begin{cases} v_{\text{omin}}^* = -NV_b - \min\left(v_{\text{dk}}^*\right) \\ v_{\text{omax}}^* = NV_b - \max\left(v_{\text{dk}}^*\right). \end{cases} \tag{3}$$

In repetitive conditions, the total rms current I_b of all the $3N$ batteries can be expressed as

$$I_b = \sqrt{\frac{1}{T}\int_T \sum_{k=1}^{3}\sum_{n=1}^{N} i_{b,k,n}^2 dt} = \sqrt{\sum_{k=1}^{3}\sum_{n=1}^{N} I_{b,k,n}^2} \tag{4}$$

where $T = 2\pi/\omega$ is the period of the fundamental ac output frequency and $I_{b,k,n}$ is the rms current value of the nth battery in the kth phase.

III. Proposed MPPA Strategy

The proposed MPPA strategy aims to minimize the total rms current I_b of all batteries through a proper injection of the common-mode reference voltage v_o^*.

In the generic module $M_{k,n}$, the battery current $i_{b,k,n}$ is zero if the battery is bypassed, while it is equal to the arm current $\pm i_k$ if the battery is inserted. The number of inserted batteries $N_{k,\text{IN}}$ within the generic arm k depends on the reference voltage v_k^*. Hence, (4) can be rewritten as

$$I_b = \sqrt{\frac{1}{T}\int_T \sum_{k=1}^{3} N_{k,\text{IN}}.i_k^2 dt} \quad \text{with } N_{k,\text{IN}}(t) = \left|\frac{v_k^*}{V_b}\right|. \tag{5}$$

Considering (5) and (2), the following quadratic $f\left(v_o^*\right)$ to be minimized can be defined

$$f = \left|v_{d1}^* + v_o^*\right| \cdot i_1^2 + \left|v_{d2}^* + v_o^*\right| \cdot i_2^2 + \left|v_{d3}^* + v_o^*\right| \cdot i_3^2. \tag{6}$$

Equation (6) is a piecewise linear function of v_o^* with at most three breaking points, which are positioned at $-v_{d1}^*, -v_{d2}^*, -v_{d3}^*$. In order to locate the absolute minimum of the function f, the derivative of f with respect to v_o^* is considered: $\rho = \left(\delta f/\delta v_o^*\right)$. Naturally, ρ is a piecewise-constant function of v_o^*

$$\rho = \operatorname{sgn}\left(v_{d1}^* + v_o^*\right) \cdot i_1^2 + \operatorname{sgn}\left(v_{d2}^* + v_o^*\right) \cdot i_2^2 + \operatorname{sgn}\left(v_{d3}^* + v_o^*\right) \cdot i_3^2. \tag{7}$$

Among the three instantaneous current phase values i_1, i_2, i_3, let us suppose that i_1 has the highest instantaneous absolute value, i.e., $i_1^2 \geq \max\left(i_2^2, i_3^2\right)$. In this hypothesis, since $i_1 + i_2 + i_3 = 0$, it is easy to verify that $i_1^2 \geq i_2^2 + i_3^2$. This entails that in (7) the first addend $\left|v_{d1}^* + v_o^*\right| \cdot i_1^2$ is predominant and determines whether $\rho < 0$ or $\rho > 0$. Around the point $v_o^* = -v_{d1}^*$, the following conditions apply:

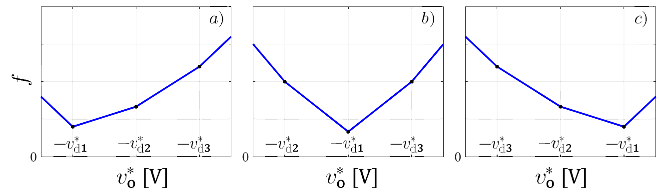

Fig. 2. Qualitative behavior of the quadratic objective function f for (a) $v_{d1}^* \geq v_{d2}^* \geq v_{d3}^*$, (b) $v_{d2}^* \geq v_{d1}^* \geq v_{d3}^*$, and (c) $v_{d3}^* \geq v_{d2}^* \geq v_{d1}^*$.

$$v_o^* < -v_{d1}^* \Longrightarrow \rho < 0; v_o^* > -v_{d1}^* \Longrightarrow \rho > 0. \tag{8}$$

Identifying the point $v_o^* = -v_{d1}^*$ as the absolute minimum of the function f as a direct consequence of the hypothesis $i_1^2 \geq \max\left(i_2^2, i_3^2\right)$.

As an example, Fig. 2 shows the qualitative behavior of f for different combinations of $v_{d1}^*, v_{d2}^*, v_{d3}^*$ values in the hypothesis $i_1^2 \geq \max\left(i_2^2, i_3^2\right)$.

As can be noted from Fig. 2, the absolute minimum of ρ is always placed at $v_o^* = -v_{d1}^*$.

Repeating the same reasoning in the hypotheses $i_2^2 \geq \max\left(i_1^2, i_3^2\right)$ and $i_3^2 \geq \max\left(i_1^2, i_2^2\right)$, it is easy to deduce that the optimum point would be $v_o^* = -v_{d2}^*$ and $v_o^* = -v_{d3}^*$ respectively. It can be concluded that the f can be minimized by setting the common-mode voltage reference equal to the voltage breaking point corresponding to the converter arm experiencing the maximum instantaneous phase current. Thus, the optimum common-mode voltage injection law can be formalized as

$$v_{\text{opt,un}}^* = \begin{cases} -v_{d1}^*, & \text{if } i_1^2 \geq \max\left(i_2^2, i_3^2\right) \\ -v_{d2}^*, & \text{if } i_2^2 \geq \max\left(i_1^2, i_3^2\right) \\ -v_{d3}^*, & \text{if } i_3^2 \geq \max\left(i_1^2, i_2^2\right). \end{cases} \tag{9}$$

As an example, steady-state sinusoidal conditions can be considered

$$v_{\text{dk}}^* = mNV_b \sin(\omega t - 2\pi(k-1)/3) \tag{10}$$
$$i_k = I \sin(\omega t - \varphi - 2\pi(k-1)/3) \tag{11}$$

where m is the modulation index, I is the peak ac current amplitude with φ as its delay angle, and ω represents the fundamental output angular frequency.

In this condition, Fig. 3(a) shows the waveforms of the optimum common-mode voltage for $m = 0.5$ and for $\varphi = \pi/4$. The correspondent phase voltages are shown in Fig. 3(b) (all voltages are normalized with respect to NV_b). Naturally, the phase-to-phase voltage resulting from Fig. 3 (which are not shown for the sake of brevity) is perfectly symmetrical and sinusoidal.

With respect to a sinusoidal and symmetrical steady-state condition, the following expression applies to the quantity I_b^2 when the optimum injection law is carried out:

$$I_{b,\text{opt,un}}^2 = \begin{cases} KmA, & \text{for } -\pi/6 + h\pi \leq \varphi \leq \pi/6 + h\pi \\ KmB & \text{for } -\pi/6 + h\pi > \varphi > \pi/6 + h\pi. \end{cases} \tag{12}$$

Authorized licensed use limited to: Universita degli Studi di Napoli Federico II. Downloaded on August 12,2026 at 12:04:15 UTC from IEEE Xplore. Restrictions apply.

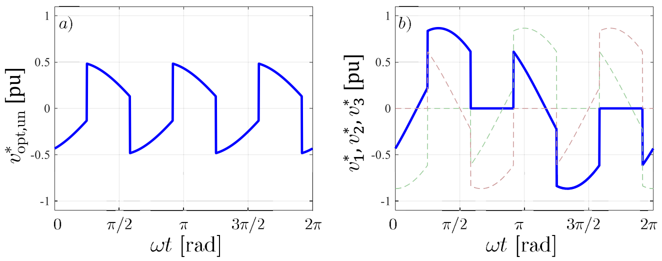

Fig. 3. (a) Optimum common-mode voltage and (b) phase voltages in presence of the optimum injection law.

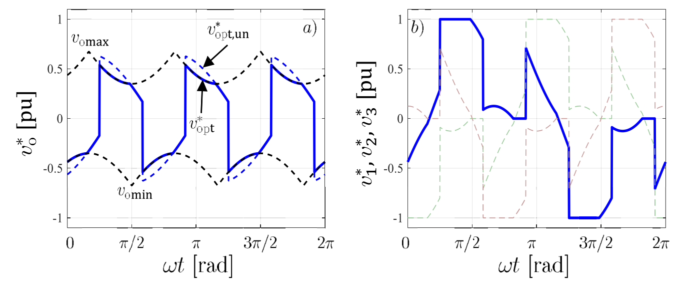

Fig. 4. (a) Unconstrained optimum common-mode voltage and its constrained version. (b) Phase voltages in presence of the optimum injection law.

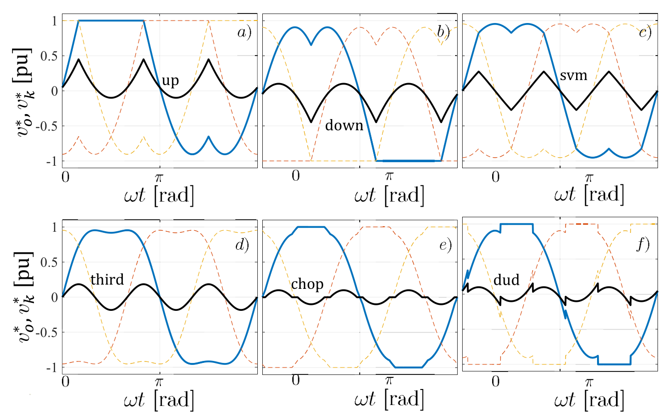

Fig. 5. Common-mode voltage for all the considered injection methods (black line) and correspondent phase voltages: (a) up, b) down, c) svm, (d) third, (e) chop, and (f) dud.

With $h \in \mathbb{Z}$ and

$$K = 3NI^2/\pi, \quad A = |\cos\varphi|$$
$$B = -\frac{2}{\sqrt{3}}|\sin\varphi| + \sqrt[3]{\cos^2\varphi}\sqrt{3} - |\cos\varphi|(1-|\sin\varphi|) + \frac{5}{2\sqrt{3}}. \tag{13}$$

As $I^2_{b,\text{opt,un}}$ has period of π, the same behavior applies for positive or negative converter output power.

It should be noted that the optimization procedure leading to (9) has been derived without taking into consideration the common-mode voltage limitations (3), resulting in an unconstrained optimum law opt, un. As a consequence, (12) represents the actual I_b^2 value only when $v^*_{\text{omin}} \le v^*_{\text{opt,un}} \le v^*_{\text{omax}}$, i.e., when the CHB arms can physically achieve the required voltages, given their limited number of modules. When this condition is not met, a constrained optimum law opt must be used instead. The opt law is the physically realizable optimal injection law, i.e., the law that ensures $v^*_{\text{omin}} \le v^*_o \le v^*_{\text{omax}}$ whilst achieving the minimization of f. The opt law can be found by noting that $v^*_{\text{opt,un}}$ defines a break-point of the function $f\left(v^*_o\right)$ for which the following relation applies:

$$v^*_o < v^*_{\text{opt,un}} \Longrightarrow \rho < 0; \quad v^*_o > v^*_{\text{opt,un}} \Longrightarrow \rho > 0. \tag{14}$$

Equation (14) ensures that when the common-mode voltage defined by the opt, un law cannot be applied, f always increases when v^*_o, while kept in the range $\left(v^*_{\text{omin}}, v^*_{\text{omax}}\right)$, moves from the nearest available value to the furthest one, even if a breaking point of f is traversed. Thus, it is possible to derive the opt common-mode voltage injection law

$$v^*_o = v^*_{\text{opt}} = \begin{cases} v^*_{\text{opt,un}}, & \text{if } \; v^*_{\text{omin}} \le v^*_{\text{opt,un}} \le v^*_{\text{omax}} \\ v^*_{\text{omax}}, & \text{if } \; v^*_{\text{opt,un}} > v^*_{\text{omax}} \\ v^*_{\text{omin}}, & \text{if } \; v^*_{\text{opt,un}} < v^*_{\text{omin}}. \end{cases} \tag{15}$$

As an example, in symmetrical sinusoidal conditions at $m = 0.65$ and $\varphi = \pi/4$, Fig. 4(a) clarifies how the unconstrained optimum common-mode voltage $v^*_{\text{opt,un}}$ is limited to the range $\left[v^*_{\text{omin}}, v^*_{\text{omax}}\right]$, obtaining the quantity v^*_{opt}. Fig. 4(b) shows the corresponding optimum phase voltages $v^*_k = v^*_{\text{dk}} + v^*_{\text{opt}}$.

The proposed technique constitutes a discontinuous modulation strategy that minimizes the total rms current I_b of all the batteries in the CHB converter architecture with reference to both steady-state or transient conditions and for any waveform of v^*_{dk} and i_k.

IV. Traditional Common-Mode Voltage Injection Methods

In order to evaluate the benefit introduced by the proposed method, several common-mode voltage injection laws are considered. With reference to a sinusoidal and symmetrical voltages set [see (10)], the common-mode voltage behavior of all injection methods at $m = 1.1$ together with the correspondent phase voltages are shown in Fig. 5 (black line). For the sake of clarity, only the first phase voltage has been depicted with a continuous line. All quantities of Fig. 5 are normalized with respect to NV_b.

In [16], the following three different methods are presented:

$$v^*_o = \begin{cases} v^*_{\text{omax}}, & \text{Up Clamping(up)} \\ v^*_{\text{omin}}, & \text{Down Clamping(down)} \\ \left(v^*_{\text{omin}} + v^*_{\text{omax}}\right)/2, & \text{SVM equivalent(svm)}. \end{cases} \tag{16}$$

The first and second lines of (16) are equal to the maximum and minimum limits of v^*_o so that the phase reference voltage references v^*_k are maximized or minimized [Fig. 5(a) and (b)]. The last line in (16) produces a quasi-triangular v^*_o waveform [see Fig. 5(c)] and is equivalent to the space vector modulation (SVM), which is often adopted for the traditional 2-level VSI.

In [19] a pure third-order harmonic injection [Fig. 5(d)] is proposed to reduce capacitor voltage ripple

Authorized licensed use limited to: Universita degli Studi di Napoli Federico II. Downloaded on August 12,2026 at 12:04:15 UTC from IEEE Xplore. Restrictions apply.

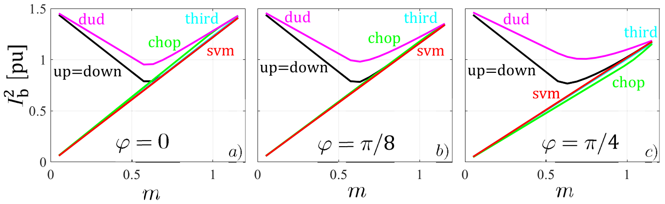

Fig. 6. Total mean square battery current for traditional methods for (a) $\varphi = 0$, (b) $\varphi = \pi/8$, and (c) $\varphi = \pi/4$.

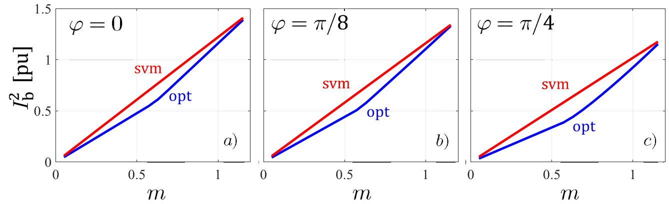

Fig. 7. Total mean square battery current for opt and svm methods for (a) $\varphi = 0$, (b) $\varphi = \pi/8$, and (c) $\varphi = \pi/4$.

in a modified MMC

$$v_o^* = \frac{|\boldsymbol{v}_{\mathbf{d}}^*| \sin(3\theta_d)}{6} \quad \text{third harmonic (third).} \tag{17}$$

With $\boldsymbol{v}_{\mathbf{d}}^* = (2/3) \sum_{k=1}^{3} v_{\mathrm{d}k}^* \cdot e^{j(2\pi(k-1))/(3)}$ the space vector of the differential voltages references.

In [21] the common-mode voltage is injected only for $m > 1$ [Fig. 5(e)] chopping the maximum reference voltage to the value ± 1

$$\bar{h} = \underset{k=1,2,3}{\operatorname{argmax}}(|v_{\mathrm{d}k}|) \tag{18}$$

$$v_o^* = \begin{cases} 1 - v_{\mathrm{d}\bar{h}}, & \text{if } v_{\mathrm{d}\bar{h}} > NV_b \\ -1 - v_{\mathrm{d}\bar{h}}, & \text{if } v_{\mathrm{d}\bar{h}} < -NV_b \\ 0, & \text{otherwise} \end{cases} \quad \text{Chopping(chop).} \tag{19}$$

In [18], a discontinuous up/down (dud) modulation is proposed [Fig. 5(f)] to reduce voltage ripple in MMC equipped with capacitors

$$\bar{k} = \underset{k=1,2,3}{\operatorname{argmax}}(|i_k|); \quad \bar{\bar{k}} = \underset{k \neq \bar{k}}{\operatorname{argmax}}(|i_k|) \tag{20}$$

$$v_{o,\mathrm{dud},a}^* = \operatorname{sign}(v_{\mathrm{d}\bar{k}}) - v_{\mathrm{d}\bar{k}}; \quad v_{o,\mathrm{dud},b}^* = \operatorname{sign}\left(v_{\mathrm{d}\bar{\bar{k}}}\right) - v_{\mathrm{d}\bar{\bar{k}}} \tag{21}$$

$$v_{o,\mathrm{dud}}^* = \begin{cases} v_{o,\mathrm{dud},a}^*, & \text{if } \left|v_{\mathrm{d}k} + v_{\mathrm{o,dud,a}}^*\right| \leq NV_{\mathrm{b}} \\ v_{o,\mathrm{dud},b}^*, & \text{otherwise} \end{cases} \quad \text{(dud).} \tag{22}$$

The waveform of $v_{o,\mathrm{dud}}^*$ naturally depends on the behavior of the currents. As an example, Fig. 5(f) refers to a symmetrical current set [see (11)] with a φ of 10°.

The analytical expressions of the total mean square battery current I_b^2 for all traditional injections methods have been calculated and reported in the Appendix.

The graphical behavior of I_b^2 for all traditional injections methods is shown in Fig. 6 as a function of the m and for three different φ; all quantities are normalized with respect to K. For the sake of clarity, different colors have been used: up and down: black; svm: red; third: cyan; chop: green; dud: magenta.

As can be noted from Fig. 6, up, down, and dud injections produce the highest I_b^2 value. svm, third, and chop methods, instead, offer better results. While $I_{b,\mathrm{svm}}^2$ and $I_{b,\mathrm{third}}^2$ are very similar for all power factors (with $I_{b,\mathrm{svm}}^2$ slightly lower), $I_{b,\mathrm{dud}}^2$ is higher at a high power factors [Fig. 6(a) and (b)]. Therefore, the svm technique is chosen as a comparison method for the proposed technique.

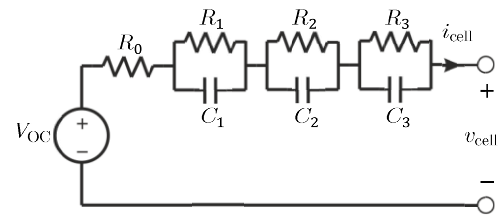

Fig. 8. Randles dynamic $3p3z$ model of a battery cell.

V. Comparison Between Traditional and Proposed Injection Methods

A fast comparison between svm and opt methods can be performed by calculating I_b^2 of (12) and (35). For example, at $m = 0.5$ and $\varphi = 0$, it result $I_{b,\mathrm{svm}}^2 \cong 0.64K$ and $I_{b,\mathrm{opt}}^2 = 0.5\ K$, testifying a reduction of about 22% in favor of the proposed method. For a wider range graphical comparison, Fig. 7 shows the I_b^2 behavior (normalized with respect to K) for svm and opt methods as function of the m and for three different φ values.

To evaluate the energy-saving benefits in the specific context of a battery-fed CHB, it is useful to introduce a battery model. The Randles dynamic $3p3z$ battery cell model shown in Fig. 8 was experimentally validated in [23] to calculate the battery energy loss in BEVs.

As demonstrated in [23], the LF current harmonics pass through the capacitances C_1–C_3, whereas the dc component is conducted through the resistors $R_1 R_3$. Naturally, the resistance R_0 conducts the total battery current.

Hence, for the generic $M_{k,n}$ module, the battery loss $P_{\mathrm{bl},k,n}$ of the nth battery in the kth phase, can be expressed by

$$P_{\mathrm{bl},k,n} = R_0 \cdot I_{b,k,n}^2 + (R_1 + R_2 + R_3) \cdot I_{b,\mathrm{dc},k,n}^2 \tag{23}$$

where $I_{b,\mathrm{dc},k,n}$ is the dc component current value of the nth battery in the kth phase while $I_{b,k,n}$ is the total rms current value (dc + ac components).

The total battery loss P_{bl} can be obtained using

$$I_b^2 = \sum_{k=1}^{3} \sum_{n=1}^{N} I_{b,k,n}^2; \quad I_{b,\mathrm{dc}}^2 = \sum_{k=1}^{3} \sum_{n=1}^{N} I_{b,\mathrm{dc},k,n}^2 \tag{24}$$

it results

$$P_{\mathrm{bl}} = R_0 I_b^2 + (R_1 + R_2 + R_3) I_{b,\mathrm{dc}}^2. \tag{25}$$

With reference to (25), as already discussed, the proposed method guarantees the minimization of the I_b^2 term (Fig. 7). For the $I_{b,\mathrm{dc}}^2$ term, it can be shown that the load power

Authorized licensed use limited to: Universita degli Studi di Napoli Federico II. Downloaded on August 12,2026 at 12:04:15 UTC from IEEE Xplore. Restrictions apply.

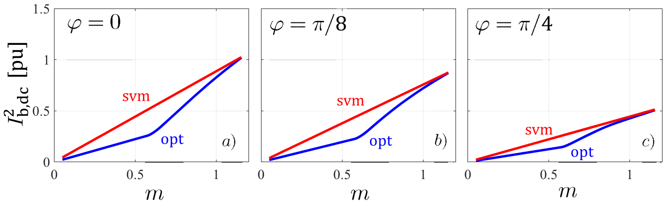

Fig. 9. Total square battery dc current component for opt and svm methods for (a) $\varphi = 0$, (b) $\varphi = \pi/8$, and (c) $\varphi = \pi/4$.

only fixes the sum of all the $I_{b,\mathrm{dc},k,n}$ values, but not each $I_{b,\mathrm{dc},k,n}$ value. To find the minimum $I^2_{b,\mathrm{dc}}$, all $I_{b,\mathrm{dc},k,n}$ should be equal (i.e., independent of k and n) which is, of course, not possible for the CHB converter where each module is switched differently. Nevertheless, from the results of numerical simulations, it is observed that the proposed opt method acts in favor of a $I_{b,\mathrm{dc},k,n}$ equalization and, in comparison with the svm method, obtains a reduction of the $I^2_{b,\mathrm{dc}}$ term. The $I^2_{b,\mathrm{dc}}$ behavior (normalized with respect to K) is shown in Fig. 9 for svm and opt methods as a function of the m and for three different φ values.

Fig. 9(c) shows $I^2_{b,\mathrm{dc}}$ equal to zero for both opt and svm methods because, as expected, at $\varphi = \pi/2$ the batteries do not supply active power $\left(I_{b,\mathrm{dc},k,n} = 0 \,\forall\, k, n\right)$.

The battery loss reduction can be evaluated by introducing the following "energy saving" metric ES

$$\mathrm{ES} = 100\cdot\left(E^{\mathrm{svm}}_{\mathrm{lb}} - E^{\mathrm{opt}}_{\mathrm{lb}}\right)/E^{\mathrm{svm}}_{\mathrm{lb}} \tag{26}$$

where $E^{\mathrm{svm}}_{\mathrm{bl}}$ and $E^{\mathrm{opt}}_{\mathrm{bl}}$ are the battery energy loss obtained with respectively the svm and the opt methods

$$E^{\mathrm{svm}}_{\mathrm{bl}} = \int P^{\mathrm{svm}}_{\mathrm{bl}} \cdot dt; \quad E^{\mathrm{opt}}_{\mathrm{bl}} = \int P^{\mathrm{opt}}_{\mathrm{bl}} \cdot dt. \tag{27}$$

The ES gives the percentage reduction of the battery energy loss obtained by the proposed opt method compared to traditional svm methods. ES depends on the m and φ. Additionally, since in (25) the two power losses contribution related to I^2_b and $I^2_{b,\mathrm{dc}}$ are weighted, respectively, by R_0 and $(R_1 + R_2 + R_3)$, ES depends on the following ratio r:

$$r = R_0/(R_0 + R_1 + R_2 + R_3). \tag{28}$$

With reference to steady-state condition, the behavior of ES, parametrized on different r values, is shown in Fig. 10 as a function of the m and for four different φ.

The energy-saving can be quite significant, depending on the operating condition and on the battery parameters. Below $m \cong 0.6$, ES is above 20% for any r and φ value, and reaches about 60% for very low power factor. The dependence on the ratio r is more evident at higher power factor, because, as previously mentioned, as $\varphi \to \pi/2$ the batteries do not supply active power $\left(I^2_{b,\mathrm{dc}} \to 0\right)$. At higher modulation indices, the ES value decreases due to the limitation on the injectable common-mode voltage. Nevertheless, even at the maximum $m = 2/\sqrt{3}$, the optimum strategy still guarantees a reduction in the range of 1%–7% depending on the power factor.

As both I^2_b and $I^2_{b,\mathrm{dc}}$ do not change with a φ shift of π; the same result applies to the charging and discharging operation. It should be noted that in the present discussion,

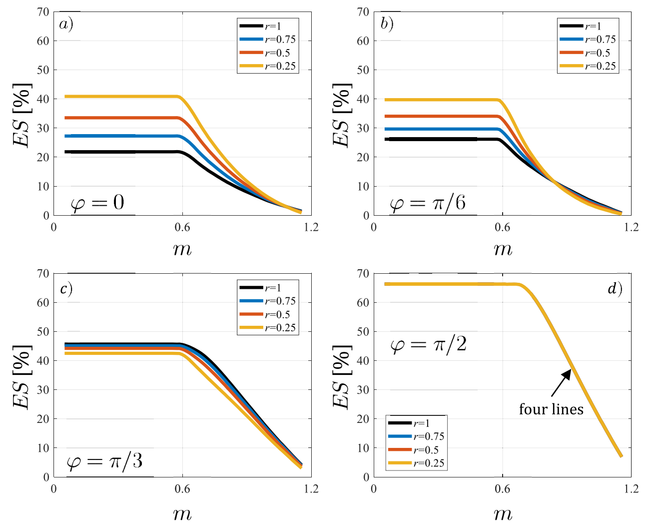

Fig. 10. Energy saving obtainable by the proposed opt technique for (a) $\varphi = 0$, (b) $\varphi = \pi/6$, (c) $\varphi = \pi/3$, and (d) $\varphi = \pi/2$.

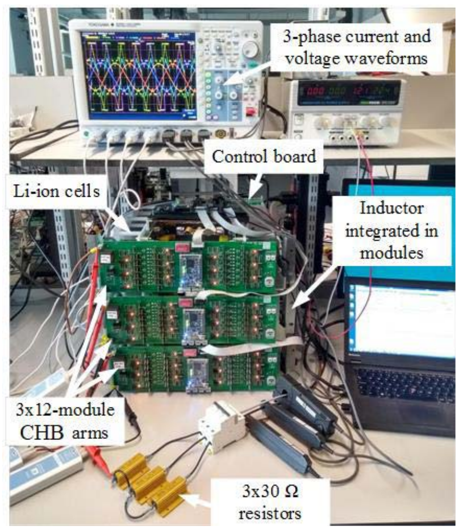

Fig. 11. Experimental setup.

the contribution of the balancing action to the battery power losses has been neglected (see Appendix).

Given the energy-saving variability, in order to better evaluate the benefit introduced by the proposed method for practical applications, two case studies are presented in Section VII.

VI. Experiments

To experimentally validate the current reduction introduced by the proposed common-mode voltage injection law, a three-phase battery-fed CHB battery is used. Each phase comprises twelve H-bridge modules which, for the sake of simplicity, are driven by the NLC technique. Each module contains a single 20 Ah lithium-titanate-oxide (LTO) cell. The experimental setup is presented in Fig. 11 (a detailed description of the hardware and control architecture is given in [24]).

Four tests are performed at 50 Hz fundamental frequency steady-state condition for different m and power factor values (see Table I).

Authorized licensed use limited to: Universita degli Studi di Napoli Federico II. Downloaded on August 12,2026 at 12:04:15 UTC from IEEE Xplore. Restrictions apply.

TABLE I
TESTS CONDITIONS

Test n	1	2	3	4
m	0.45	0.45	0.9	0.9
$\cos\varphi$	1	0.7	1	0.7

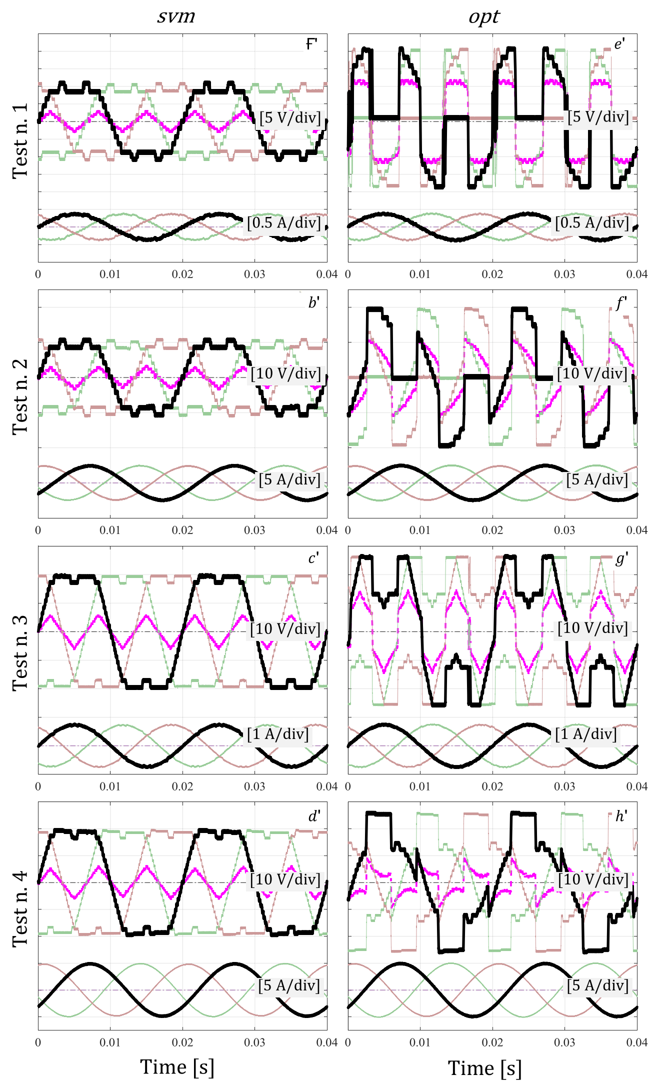

Fig. 12. Experimental phase voltages and currents for all tests. svm method: (a) Test 1, (b) Test 2, (c) Test 3, and (d) Test 4; opt method: (e) Test 1, (f) Test 2, (g) Test 3, and (h) Test 4.

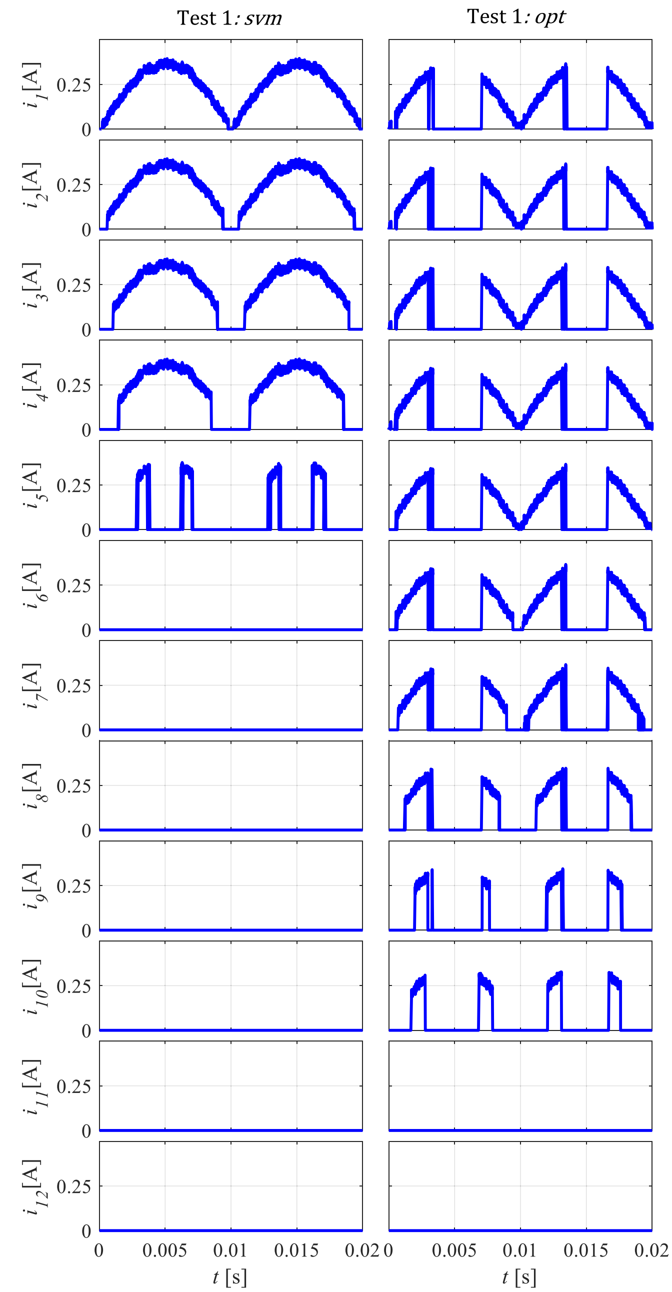

Fig. 13. Experimental behavior of 12 cells currents during Test 1.

To achieve the two values of the power factor a different combination of inductors and resistors is used: $L = 2.94$ mH, $R = 30\ \Omega$ for $\cos\varphi \cong 1$ and $L = 10.3$ mH, $R = 3\ \Omega$ for $\cos\varphi \cong 0.7$. The four tests are repeated for opt and svm methods, resulting in a total of eight experiments.

The three-phase voltages and currents are sampled by the oscilloscope at 2.5 MS/s. These, together with the common-mode voltage, are shown in Fig. 12 for all eight experiments. For clarity, the first phase voltage and current have been depicted with a thick black line and the magenta line represents the common-mode component. As can be seen, the load currents are substantially sinusoidal and symmetrical for all eight tests, with an amplitude only dependent on the operating condition. This confirms that the load voltages are not affected by the common-mode voltage component.

The 36 cell currents $i_{b,k,n}$ (with $k = 1, 2, 3$ and $n = 1, \ldots, 12$) are derived from the measured phase currents using the control switching signals. Each cell rms current value $I_{b,k,n}$ and dc current component $I_{b,\mathrm{dc},k,n}$ is then calculated, and the quantities I_b^2 and $I_{b,\mathrm{dc}}^2$ are obtained as per (24).

For the sake of brevity, only first phase of Tests 1 and 3 individual cell current behavior is shown in Figs. 13 and 15. From Fig. 13, it can be noted that for the svm method only cells from 1 to 5 contribute to the load power, while the cells from 6 to 12 are completely disconnected. On the contrary,

Authorized licensed use limited to: Universita degli Studi di Napoli Federico II. Downloaded on August 12,2026 at 12:04:15 UTC from IEEE Xplore. Restrictions apply.

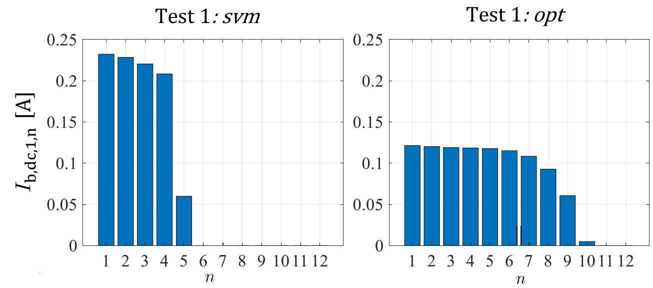

Fig. 14. Mean values of 12 cells currents during Test 1.

TABLE II
TESTS RESULTS

Test n.		*Svm method* exp	*Svm method* num	*Opt method* exp	*Opt method* num	***ES*** [%]
1	I_{b}^2[pu]	0.555	0.575	0.456	0.450	18-47
	$I_{\mathrm{b,dc}}^2$[pu]	0.394	0.408	0.207	0.211	
2	I_{b}^2[pu]	0.489	0.478	0.320	0.316	35-43
	$I_{\mathrm{b,dc}}^2$[pu]	0.208	0.200	0.118	0.116	
3	I_{b}^2[pu]	1.12	1.15	1.03	1.06	9-15
	$I_{\mathrm{b,dc}}^2$[pu]	0.817	0.834	0.695	0.725	
4	I_{b}^2[pu]	0.981	0.956	0.824	0.813	8-16
	$I_{\mathrm{b,dc}}^2$[pu]	0.427	0.409	0.393	0.381	

the opt method tends to spread the power contribution among a higher number of cells. This situation corresponds to the mean current of the cells ($I_{b,\mathrm{dc},1,n}$) as shown in Fig. 14, which verifies the efficacy of the proposed technique to act in favor of a $I_{b,\mathrm{dc},k,n}$ equalization, which ultimately reduces the $I_{b,\mathrm{dc}}^2$ term. The same considerations can be applied to Figs. 15 and 16.

The experimental (exp) values of the I_b^2 and $I_{b,\mathrm{dc}}^2$ (normalized with respect to K) are summarized in Table II for all experimental tests. To corroborate the previous numerical analysis, the numerical (num) values of the I_b^2 and $I_{b,\mathrm{dc}}^2$ are also exhibited. Moreover, according to the Randles dynamic $3p3z$ battery cell model shown in Fig. 8, the obtainable energy-saving range is reported in the last column.

With reference to Table II, the good agreement between the values reported in columns "exp" and "num" testifies the efficacy of the theoretical analysis (within the experimental error due to current measurement). In comparison with the svm method, the proposed technique demonstrates a substantial reduction of both the I_b^2 and $I_{b,\mathrm{dc}}^2$ quantities, resulting in a significant ES range.

As previously clarified, the exact value of the obtainable ES eventually depends on the battery parameter r defined in (28).

VII. CASE STUDIES

To better evaluate the potential ES obtainable from the proposed technique in a real-world application, an ESS and a BEV are considered and numerically evaluated in MATLAB/Simulink environment. In both cases, a 12 module per arm CHB converter is modulated using phase-disposition 10 kHz PWM, and the battery losses are computed by means of the instantaneous currents flowing in the R_0, R_1, R_2, R_3 resistances of the Randles dynamic battery cell model. The battery pack is based on the parameters for an ANR26650M1A cell which are available in [23].

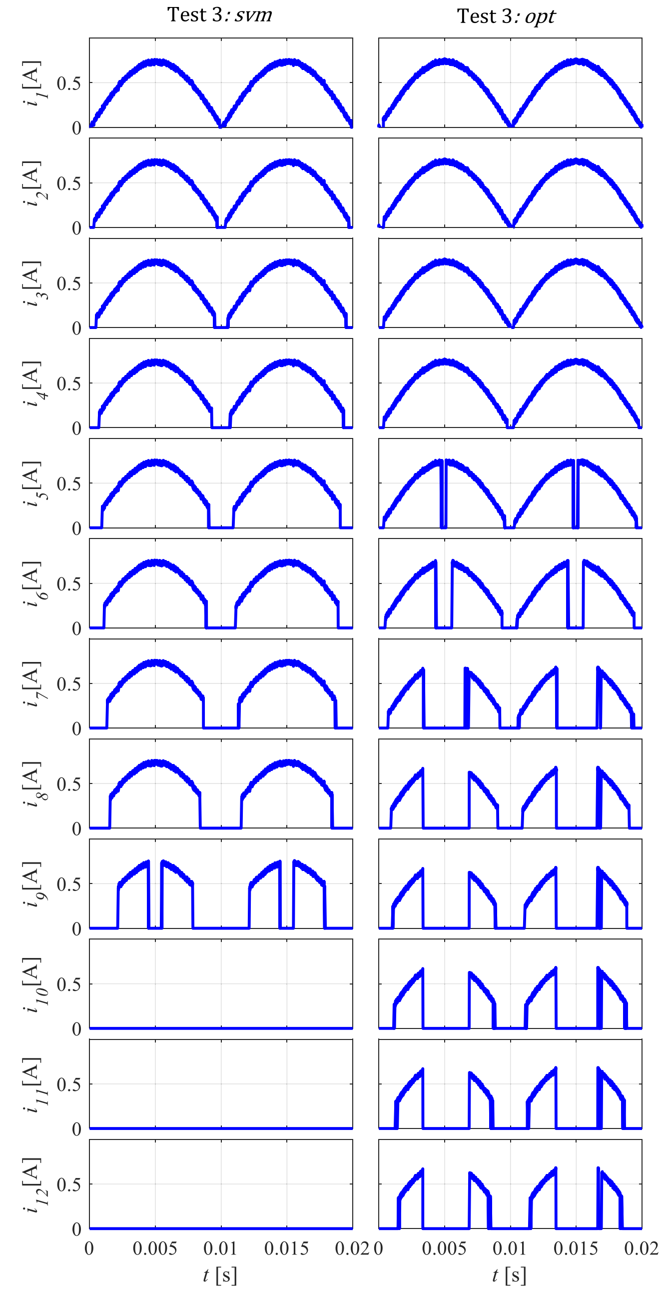

Fig. 15. Experimental behavior of 12 cells currents during Test 3.

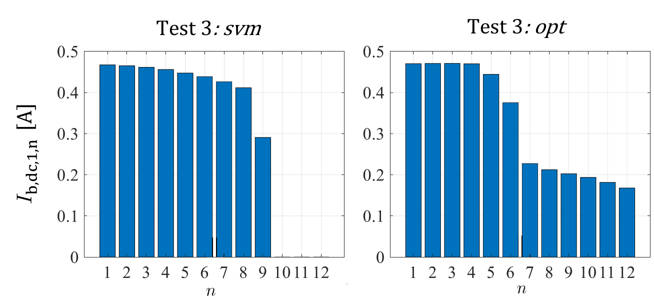

Fig. 16. Mean values of 12 cells currents during Test 3.

Authorized licensed use limited to: Universita degli Studi di Napoli Federico II. Downloaded on August 12,2026 at 12:04:15 UTC from IEEE Xplore. Restrictions apply.

TABLE III
BEV OPERATION OVER ONE WLTP CYCLE

Vehicle type	Nissan Leaf	Converter output energy	2530 Wh
Rated power	110 kW	Switching loss	4.6 Wh
Rated voltage	220 V	Conduction loss	114.0 Wh
Storage energy	40 kWh	$E_{\mathrm{lb}}^{\mathrm{svm}}$	188.2 Wh
Modules per arm	12	$E_{\mathrm{lb}}^{\mathrm{opt}}$	136.4 Wh
Cell type	ANR26650M1A	$E_{\mathrm{lb}}^{\mathrm{svm}} - E_{\mathrm{lb}}^{\mathrm{opt}}$	51.8 Wh
Switch type	AUIRF8739L2TR	***ES***	**27.5 %**

TABLE IV
ESS APPLICATION

Rated power	3 MW	Switching loss	3.53 kWh
Rated voltage	11 kW	Conduction loss	12.2 kWh
Storage energy	3 MWh	$E_{\mathrm{lb}}^{\mathrm{svm}}$	27.6 kWh
Modules per arm	12	$E_{\mathrm{lb}}^{\mathrm{opt}}$	24.6 kWh
Cell type	ANR26650M1A	$E_{\mathrm{lb}}^{\mathrm{svm}} - E_{\mathrm{lb}}^{\mathrm{opt}}$	3.0 kWh
Switch type	SKM200GB17E4	***ES***	**10.9 %**

Converter conduction losses P_c have been calculated as

$$P_c = 3N(V_t + R_c I)I \tag{29}$$

where V_t is the fixed forward/reverse voltage of the power module, (i.e., the power switch/reverse diode fixed ON-state voltage drop), R_c is the forward/reverse resistance of the power module (i.e., power switch/reverse diode forward resistance).

To calculate the switching losses P_{sw}, the variation of the current and the voltage is considered linear in a switching interval (this assumption allows the computation of the switching energy with a good accuracy)

$$P_{\mathrm{sw}} = (2/\pi) f_{\mathrm{sw}}(t_{\mathrm{ON}} + t_{\mathrm{OFF}})\mathrm{I}V_b \tag{30}$$

where f_{sw} is the switching frequency, and t_{ON} and t_{OFF} are the ON and OFF times, respectively.

A. BEV Application

A 110 kW/40 kWh BEV is driven by a CHB equipped with International Rectifier AUIRF8739L2TR MOSFETs. The main parameters of the system are derived directly from the 110 kW version of the Nissan Leaf. The numerical investigation is performed with reference to the worldwide harmonized light vehicle testing procedure (WLTP) driving cycle [25] and repeated for both svm and opt methods. The main system characteristics and results are summarized in Table III.

The battery losses are comparable with the total MOSFET losses. The reduction of the battery losses obtained using the proposed opt modulation method is significant (27.5%). This large saving is due to the nature of the application: given the speed profile associated with the driving cycle, the motor works mainly either at low m/high power factor or at high m/low power factor. The reduction of the battery losses leads to a tangible gain in the battery pack efficiency, which, increases from about 93.3% to about 95.1% under the considered test conditions.

B. ESS Application

A 3 MW, 3 MWh ESS equipped with Semikron SKM200GB17E4 IGBTs and connected to a medium voltage grid of 11 kV is considered. The ESS undergoes a complete charge/discharge cycle at rated power at unity power factor whilst adapting the m to maintain a constant output voltage of 11 kV as the battery pack is charged/discharged (and so the cell voltage varies). The simulation is repeated for both svm and opt method, and the main results are reported in Table IV, together with the system main data.

The energy-saving is lower than that found for the BEV case because the ESS application is characterized by higher m values and operates at unitary power factor.

VIII. CONCLUSION

This work presents a novel MPPA modulation strategy for three-phase, single-star CHB converters with distributed dc sources. Exploiting the degree of freedom in the voltage shared by all phases, an optimum common-mode voltage injection law has been derived, which minimizes the sum of the rms current flowing through each dc source. The technique significantly reduces the sum of the square of dc current components flowing in each dc sources such as batteries, which exhibit dynamic *RC*-type behavior. This reduces the loss in the battery and hence prolongs the battery life. The proposed method could be implemented in other types of modular multilevel cascaded converter.

Experimental tests on a 36-cell full-bridge CHB converter validate the simulations and numerical derivations. The obtainable battery energy-saving is dependent on the battery parameters and on the converter m and power factor. Using previously validated battery cell parameters, BEV and ESS applications have been investigated, showing that significant ESs can be achieved if the proposed modulation technique is applied.

APPENDIX

With reference to a sinusoidal and symmetrical currents set [see (11)], the conditions $v_o^* = v_{\mathrm{omax}}^*$ (up injection) and $v_o^* = v_{\mathrm{omin}}^*$ (*down* method) result in the same I_b^2 expression

$$\begin{aligned} I_{b,\mathrm{up}}^2 &= I_{b,\mathrm{down}}^2 \\ &= \begin{cases} K\left(\pi/2 - 3\sqrt{3}/4\right), & \text{for} \quad m \le 1/\sqrt{3} \\ KC, & \text{for} \quad 1/\sqrt{3} < m \le 2/3 \\ KD, & \text{for} \quad m > 2/3. \end{cases} \end{aligned} \tag{31}$$

With:

$$C = \left[\begin{array}{l} \left[2 + \left(\dfrac{1}{3} - \dfrac{1}{9m^2}\right)\cos(2\varphi)\right]\sqrt{(3m^2-1)} \\ -2\arccos\left(\dfrac{1}{m\sqrt{3}}\right) + \dfrac{\left(2\pi - 3\sqrt{3}\right)}{4} \end{array}\right] \tag{32}$$

$$D = \left[\begin{array}{l} \left[2\sqrt{(3m^2-1)^3} + \sqrt{3}(9m^2 - 6m^3 - 2)\right]\dfrac{\cos(2\varphi)}{36m^2} \\ + \dfrac{12\sqrt{(3m^2-1)} + 4\pi - 3\sqrt{3}\ m}{12} - \arccos\left(\dfrac{1}{m\sqrt{3}}\right) \end{array}\right]. \tag{33}$$

Authorized licensed use limited to: Universita degli Studi di Napoli Federico II. Downloaded on August 12,2026 at 12:04:15 UTC from IEEE Xplore. Restrictions apply.

$$
\begin{aligned}
I^2_{b,\text{dud},1} &= K\left(\frac{\pi}{2} - m\cos\varphi\right)\\
I^2_{b,\text{dud},2} &= K\left[2\bar{\alpha} - \frac{\pi}{2} - m\cos\varphi + 2E(18 + F\cos(2\varphi - \pi/3))\right]\\
I^2_{b,\text{dud},3} &= K\left[2\bar{\alpha} - \frac{\pi}{2} + \frac{\sqrt{3}}{2} + \sqrt{3}\ G\cos(2\varphi) - 3m\cos\varphi + E(36 + F\cos(2\varphi))\right]\\
I^2_{b,\text{dud},4} &= K\left[2\bar{\alpha} - \frac{\pi}{2} - m\cos\varphi + 2E\left(18 + F\cos\left(2\varphi + \frac{\pi}{3}\right)\right)\right]\\
I^2_{b,\text{dud},5} &= K\left[\bar{\alpha} - \varphi - \frac{\pi}{3} + \frac{\sqrt{3}}{2} + G\sin\left(2\varphi + \frac{\pi}{3}\right) - m\left(\cos\varphi + 4\cos\left(\varphi + \frac{\pi}{3}\right)\right)\Big/3 + E\left(18 + F\cos\left(2\varphi + \frac{\pi}{3}\right)\right)\right]\\
I^2_{b,\text{dud},6} &= I^2_{\text{b,dud},3}\\
I^2_{b,\text{dud},7} &= K\left[\bar{\alpha} - \varphi - \frac{\pi}{3} + \frac{\sqrt{3}}{2} + G\sin\left(2\varphi + \frac{\pi}{3}\right) - m\left(\cos\varphi + 4\cos\left(\varphi - \frac{\pi}{3}\right)\right)\Big/3 + E\left(18 + F\cos\left(2\varphi - \frac{\pi}{3}\right)\right)\right]\\
E &= \frac{\sqrt{3m^2-1}}{18};\quad F = \frac{(6m^2-2)}{m^2};\ G = \frac{(9m^2-2)}{18m^2}\\
H &= \frac{\sqrt{m^2-1}}{3};\quad \bar{\alpha} = \sin^{-1}\left(\frac{1}{\sqrt{3}m}\right)
\end{aligned}
\tag{38}
$$

From the svm and third injection, instead, it is,

$$I^2_{b,\text{third}} = Km\left(\frac{19}{18} + \frac{7\cos(2\varphi)}{30}\right) \tag{34}$$

$$I^2_{b,\text{svm}} = Km\left[\left(3-\sqrt{3}\right)\frac{\cos(2\varphi)}{6} + \frac{\left(6-\sqrt{3}\right)}{4}\right]. \tag{35}$$

For the chop method it is,

$$
I^2_{b,\text{chop}} = \begin{cases} Km(1+\cos(2\varphi)/3), & \text{for } m \le 1\\ K\left[\begin{array}{l}\sin^{-1}\left(\frac{1}{m}\right) - \frac{\pi}{2} + m\left(\frac{\cos(2\varphi)}{3}+1\right)\\ +\sqrt{H}\left(1 - 2H\frac{\cos(2\varphi)}{3m^2}\right)\end{array}\right], & \text{for } m > 1. \end{cases}
\tag{36}
$$

Finally, the dud method gives

$$
I^2_{b,\text{dud}} = \begin{cases}
I^2_{b,\text{dud},1}, & \text{for } m \le 1/\sqrt{3}\\
I^2_{b,\text{dud},2}, & \text{for } 1/\sqrt{3} < m \le 2/3 \text{ and } \varphi < \bar{\alpha} - \pi/2\\
I^2_{b,\text{dud},3}, & \text{for } 1/\sqrt{3} < m \le 2/3 \text{ and } |\varphi| \le \pi/2 - \bar{\alpha}\\
I^2_{b,\text{dud},4}, & \text{for } 1/\sqrt{3} < m \le 2/3 \text{ and } \varphi > \pi/2 - \bar{\alpha}\\
I^2_{b,\text{dud},5}, & \text{for } m > 2/3 \text{ and } \varphi < \pi/6 - \bar{\alpha}\\
I^2_{b,\text{dud},6}, & \text{for } m > 2/3 \text{ and } |\varphi| \le \bar{\alpha} - \pi/6\\
I^2_{b,\text{dud},7}, & \text{for } m > 2/3 \text{ and } \varphi > \bar{\alpha} - \pi/6
\end{cases}
\tag{37}
$$

where, (38), as shown at the top of the page.

In this work, all the batteries (dc sources) in each CHB module are assumed to be perfectly balanced so that they have the same voltage V_b. Battery SoC balancing within an arm can be achieved by sorting approaches. The sorting does not influence the total battery loss because it does not change the number of cells conducting current at any one time; this is determined only by the arm voltage reference. The inter-arm balancing can be achieved by adding a fundamental component $v^*_{o,\text{bal}}$ to the common-mode voltage calculated as part of the opt method. In this case, the limits (3) for the common-mode voltage modify as follows:

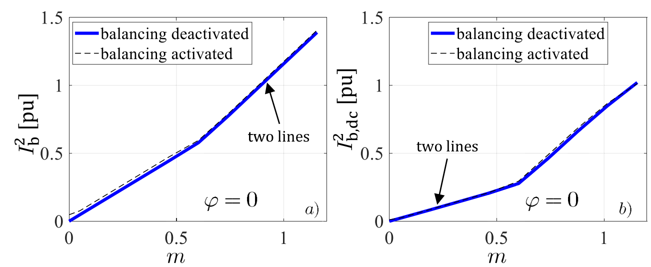

Fig. 17. Effect of the balancing action on (a) I^2_b and (b) $I^2_{b,\text{dc}}$ for opt method.

$$
\begin{cases}
v^*_{\text{omin}} = -NV_b - \min\left(v^*_{\text{dk}}\right) - \min\left(v^*_{o,\text{bal}}\right)\\
v^*_{\text{omax}} = NV_b - \max\left(v^*_{\text{dk}}\right) - \max\left(v^*_{o,\text{bal}}\right).
\end{cases}
\tag{39}
$$

Due to the slow evolution of battery SoC, a strong and fast balancing action is not normally needed, i.e., the magnitude of the balancing power can be chosen as a few percent of the rated value, producing a minor effect on the battery losses. For example, fixing $v^*_{o,\text{bal}}$ at 5% of NV_b for $\varphi = 0$, the quantities I^2_b and $I^2_{b,\text{dc}}$ obtained from the opt method are shown in Fig. 17(a) and (b) with balancing action deactivated (blue lines) and activated (black dashed lines).

This indicates that the extra loss due to balancing action may be neglected; similar results have been found for different φ values.

Authorized licensed use limited to: Universita degli Studi di Napoli Federico II. Downloaded on August 12,2026 at 12:04:15 UTC from IEEE Xplore. Restrictions apply.

REFERENCES

[1] M. Espinoza, R. Cárdenas, M. Díaz, and J. C. Clare, "An enhanced *dq*-based vector control system for modular multilevel converters feeding variable-speed drives," *IEEE Trans. Ind. Electron.*, vol. 64, no. 4, pp. 2620–2630, Apr. 2017.

[2] L. H. S. C. Barreto, D. de A. Honorio, D. de Souza Oliveira, and P. P. Praça, "An interleaved-stage AC–DC modular cascaded multilevel converter as a solution for MV railway applications," *IEEE Trans. Ind. Electron.*, vol. 65, no. 4, pp. 3008–3016, Apr. 2018.

[3] L. Zhang, Y. Tang, S. Yang, and F. Gao, "Decoupled power control for a modular-multilevel-converter-based hybrid AC–DC grid integrated with hybrid energy storage," *IEEE Trans. Ind. Electron.*, vol. 66, no. 4, pp. 2926–2934, Apr. 2019.

[4] N. Li, F. Gao, T. Hao, Z. Ma, and C. Zhang, "SOH balancing control method for the MMC battery energy storage system," *IEEE Trans. Ind. Electron.*, vol. 65, no. 8, pp. 6581–6591, Aug. 2018.

[5] B. Novakovic and A. Nasiri, "Modular multilevel converter for wind energy storage applications," *IEEE Trans. Ind. Electron.*, vol. 64, no. 11, pp. 8867–8876, Nov. 2017.

[6] M. A. Parker, L. Ran, and S. J. Finney, "Distributed control of a fault-tolerant modular multilevel inverter for direct-drive wind turbine grid interfacing," *IEEE Trans. Ind. Electron.*, vol. 60, no. 2, pp. 509–522, Feb. 2013.

[7] P. M. Meshram and V. B. Borghate, "A simplified nearest level control (NLC) voltage balancing method for modular multilevel converter (MMC)," *IEEE Trans. Power Electron.*, vol. 30, no. 1, pp. 450–462, Jan. 2015.

[8] E. Chatzinikolaou and D. J. Rogers, "Cell SoC balancing using a cascaded full-bridge multilevel converter in battery energy storage systems," *IEEE Trans. Ind. Electron.*, vol. 63, no. 9, pp. 5394–5402, Sep. 2016.

[9] M. Quraan, T. Yeo, and P. Tricoli, "Design and control of modular multilevel converters for battery electric vehicles," *IEEE Trans. Power Electron.*, vol. 31, no. 1, pp. 507–517, Jan. 2016.

[10] F. Deng, Y. Tian, R. Zhu, and Z. Chen, "Fault-tolerant approach for modular multilevel converters under submodule faults," *IEEE Trans. Ind. Electron.*, vol. 63, no. 11, pp. 7253–7263, Nov. 2016.

[11] M. Aleenejad, H. Mahmoudi, S. Jafarishiadeh, and R. Ahmadi, "Fault-tolerant space vector modulation for modular multilevel converters with bypassed faulty submodules," *IEEE Trans. Ind. Electron.*, vol. 66, no. 3, pp. 2463–2473, Mar. 2019.

[12] Y. Li, Y. Wang, and B. Q. Li, "Generalized theory of phase-shifted carrier PWM for cascaded H-bridge converters and modular multilevel converters," *IEEE J. Emerg. Sel. Topics Power Electron.*, vol. 4, no. 2, pp. 589–605, Jun. 2016, doi: 10.1109/JESTPE.2015.2476699.

[13] H. Akagi, "Classification, terminology, and application of the modular multilevel cascade converter (MMMC)," *IEEE Trans. Power Electron.*, vol. 26, no. 11, pp. 3119–3130, Nov. 2011.

[14] M. Quraan, P. Tricoli, S. D'Arco, and L. Piegari, "Efficiency assessment of modular multilevel converters for battery electric vehicles," *IEEE Trans. Power Electron.*, vol. 32, no. 3, pp. 2041–2051, Mar. 2017.

[15] E. Chatzinikolaou and D. J. Rogers, "A comparison of grid-connected battery energy storage system designs," *IEEE Trans. Power Electron.*, vol. 32, no. 9, pp. 6913–6923, Sep. 2017.

[16] B. M. Shihab, H. S. Che, and W. P. Hew, "Symmetrical six-phase PWM methods using similar and dissimilar zero-sequence signals injection," in *Proc. 4th IET Clean Energy Technol. Conf. (CEAT)*, Nov. 2016, pp. 1–6, doi: 10.1049/CP.2016.1335.

[17] A. Dekka, B. Wu, V. Yaramasu, and N. R. Zargari, "Model predictive control with common-mode voltage injection for modular multilevel converter," *IEEE Trans. Power Electron.*, vol. 32, no. 3, pp. 1767–1778, Mar. 2017.

[18] R. Picas, J. Zaragoza, J. Pou, S. Ceballos, G. Konstantinou, and G. J. Capella, "Study and comparison of discontinuous modulation for modular multilevel converters in motor drive applications," *IEEE Trans. Ind. Electron.*, vol. 66, no. 3, pp. 2376–2386, Mar. 2019.

[19] M. Huang, Z. Kang, W. Li, J. Zou, X. Ma, and J. Li, "Modified modular multilevel converter with third-order harmonic voltage injection to reduce submodule capacitor voltage ripples," *IEEE Trans. Power Electron.*, vol. 36, no. 6, pp. 7074–7086, Jun. 2021, doi: 10.1109/TPEL.2020.3035286.

[20] D. Iannuzzi, M. Pagano, L. Piegari, and P. Tricoli, "Current balancing of cascaded H-bridge converters for PV systems with partial shading," *COMPEL, Int. J. Comput. Math. Electr. Electron. Eng.*, vol. 34, no. 6, pp. 1879–1895, Nov. 2015.

[21] J. Lamb, B. Mirafzal, and F. Blaabjerg, "PWM common mode reference generation for maximizing the linear modulation region of CHB converters in islanded microgrids," *IEEE Trans. Ind. Electron.*, vol. 65, no. 7, pp. 5250–5259, Jul. 2018, doi: 10.1109/TIE.2017.2777401.

[22] D. De Simone, P. Tricoli, S. D'Arco, and L. Piegari, "Windowed PWM: A configurable modulation scheme for modular multilevel converter-based traction drives," *IEEE Trans. Power Electron.*, vol. 35, no. 9, pp. 9727–9736, Sep. 2020, doi: 10.1109/TPEL.2020.2969375.

[23] O. Theliander, A. Kersten, M. Kuder, W. Han, E. A. Grunditz, and T. Thiringer, "Battery modeling and parameter extraction for drive cycle loss evaluation of a modular battery system for vehicles based on a cascaded H-bridge multilevel inverter," *IEEE Trans. Ind. Appl.*, vol. 56, no. 6, pp. 6968–6977, Nov./Dec. 2020, doi: 10.1109/TIA.2020.3026662.

[24] E. Chatzinikolaou and D. J. Rogers, "Hierarchical distributed balancing control for large-scale reconfigurable AC battery packs," *IEEE Trans. Power Electron.*, vol. 33, no. 7, pp. 5592–5602, Jul. 2018.

[25] C. Attaianese, M. Di Monaco, I. Spina, and G. Tomasso, "A variational approach to MTPA control of induction motor for EVs range optimization," *IEEE Trans. Veh. Technol.*, vol. 69, no. 7, pp. 7014–7025, Jul. 2020, doi: 10.1109/TVT.2020.2983908.

Ivan Spina was born in Naples, Italy, in July 15, 1982. He received the M.S. (*cum laude*) and Ph.D. degrees in electrical engineering from the University of Naples Federico II, Naples, Italy, in 2008 and 2012, respectively.

From 2012 to 2013, he was a Post-Doctoral Research Fellow with the Department of Electrical Engineering, University of Naples Federico II, where he has been an Assistant Professor of electrical machines and drives, since 2014. In 2017, he was invited as a Research Fellow by the Birmingham Centre for Railway Research and Education. In 2018, he joined the teaching team for the University of Birmingham program in Urban Railway Engineering, Singapore. He has authored or coauthored several scientific articles published in international journals and conference proceedings. His research interests include modeling, diagnostic, and control of power electronics and electrical drives for industrial and traction applications.

Daniel J. Rogers (Senior Member, IEEE) received the M.Eng. and Ph.D. degrees in electrical and electronic engineering from Imperial College London, London, U.K., in 2007 and 2011, respectively.

He is an Associate Professor with the Department of Engineering Science, University of Oxford, Oxford, U.K. He conducts research in collaboration with industry and has been an investigator on U.K. Engineering and Physical Science Research Council (EPSRC) research projects in the areas of power electronics, grid-scale energy storage and microgrids. His research interests in power electronics range from active control of transistor switching, to circuit and control system design, through to novel applications enabled by wide bandgap devices.

Gianluca Brando was born in Naples, Italy, in September 27, 1973. He received the M.S. (*cum laude*) and Ph.D. degrees in electrical engineering from the University of Naples Federico II, Naples, in 2000 and 2004, respectively.

From 2020 to 2021, he was an Assistant Professor of Electrical Machines and Drives with the Department of Electrical Engineering and Information Technology, University of Naples Federico II, where he has been an Associate Professor, since 2021. He was an author of several scientific articles published in international journals and conference proceedings. His research fields are focused on control strategies for renewable energy sources, modeling and control of electrical drives, multilevel converters modulation, and real-time implementations.

Dr. Brando is the Technical Program Chair of the International Symposium of Power Electronics, Electrical Drives, Automation and Motion (SPEEDAM).

Authorized licensed use limited to: Universita degli Studi di Napoli Federico II. Downloaded on August 12,2026 at 12:04:15 UTC from IEEE Xplore. Restrictions apply.

Efstratios Chatzinikolaou received the Diploma degree in electrical and computer engineering from the National Technical University of Athens, Athens, Greece, in 2013, and the D.Phil. degree in engineering science from the University of Oxford, Oxford, U.K, in 2018.

Since May 2019, he has been working as a Senior Power Electronics Engineer with Brill Power, Oxford. His research interests include modular multilevel converter topologies and power electronic interfaces for battery energy storage systems.

Yam P. Siwakoti (Senior Member, IEEE) received the B.Tech. degree in electrical engineering from the National Institute of Technology, Hamirpur, India, in 2005, the dual M.E. degree in electrical power engineering from the Norwegian University of Science and Technology, Trondheim, Norway, and Kathmandu University, Dhulikhel, Nepal, in 2010, and the Ph.D. degree in electronic engineering from Macquarie University, Sydney, Australia, in 2014.

He was a Post-Doctoral Fellow with the Department of Energy Technology, Aalborg University, Copenhagen, Denmark, from 2014 to 2016. He was a Visiting Scientist with Fraunhofer Institute for Solar Energy Systems, Freiburg, Germany, from 2017 to 2018. Currently, he is a Senior Lecturer with the Faculty of Engineering and Information Technology, University of Technology Sydney, Australia.

Dr. Siwakoti was a recipient of the prestigious Green Talent Award from the Federal Ministry of Education and Research, Germany, in 2016. He serves as an Associate Editor of three major journals of IEEE (IEEE TRANSACTIONS ON POWER ELECTRONICS, IEEE TRANSACTIONS ON INDUSTRIAL ELECTRONICS, and IEEE JOURNAL OF EMERGING AND SELECTED TOPICS IN POWER ELECTRONICS) and the IET *Power Electronics*.

Authorized licensed use limited to: Universita degli Studi di Napoli Federico II. Downloaded on August 12,2026 at 12:04:15 UTC from IEEE Xplore. Restrictions apply.